

# 3D Ultrasound Computer Tomography for Breast Cancer Diagnosis at KIT: an Overview

N.V. Ruiter<sup>1</sup>, T. Hopp<sup>1</sup>, M. Zapf<sup>1</sup>, A. Menshikov<sup>1</sup>, C. Kaiser<sup>2</sup>, H. Gemmeke<sup>1</sup>

<sup>1</sup> Karlsruhe Institute of Technology, Karlsruhe, Germany

E-mail: nicole.ruiter@kit.edu

<sup>2</sup> University Medical Center, Mannheim, Germany

## Abstract

3D Ultrasound Computer Tomography (USCT) emitting and receiving spherical wave fronts overcomes the limitations of 2D systems by offering a nearly isotropic 3D point spread function, a large depth of field, less loss of out-of-plane reflections, and fast 3D data acquisition. 3D devices for clinical practice require a more complex hard- and software due to the huge data rate, time-consuming image reconstruction, and large number of small transducers. The here reviewed KIT 3D USCT is a prototype for clinical studies, which realizes for the first time the full benefits of a 3D system.

**Keywords:** Ultrasound Computer Tomography, clinical application

## 1 Introduction

Ultrasound computer tomography (USCT) was first investigated in the 1970s, see e.g. the work by Schomberg [1]. The main advantages of such USCT systems for breast cancer detection and diagnosis are simultaneously recordings of reflection, attenuation and speed of sound images, high image quality, fast data acquisition, and no use of ionization radiation.

Building such a device for clinical practice was not successful for a long time - mostly due to the huge data rate and the time-consuming image reconstruction. Yet, promising ex-vivo results have been archived by numerous groups, e.g. [2]–[5]. Currently, the first 2D and 2.5D systems have become available for clinical evaluation [6], [7]. Usually USCT systems implement unfocused ultrasound emission and reception to reconstruct optimally focused reflection images by synthetic aperture post-beamforming. However, in most systems post-beamforming is only applied in one imaging plane. This leads to large slice thickness with

limited depth of field, loss of out-of-plane reflections, and large number of movement steps to acquire a stack of images of the whole volume [7]. 3D USCT, using spherical wave fronts for imaging, overcomes these limitations [8].

However, a 3D system requires a large number of transducers approx. two orders of magnitude larger than in a 2D system to fulfil the sampling theorem. In order to approximate a spherical wave front, the individual transducer area has to be small, which leads to low sound pressure and low signal-to-noise ratio (SNR). For in-vivo imaging, the data acquisition time has to be short to prevent image degradation by patient movement. Also, the image reconstruction using post-beamforming is very time consuming.

The current prototype for 3D USCT, the KIT 3D USCT II, is the first full 3D system for in-vivo imaging. It demonstrates that imaging with a sparse transducer setup it is possible. First clinical data showed that 3D acquisition and reconstruction of speed of sound and attenuation images give a direct access to tissue types and cancer detection as proposed by Greenleaf [9]. The prototype, the hardware setup, the image reconstruction methods and experimental and clinical results are described in this overview paper.

## 2 Methodology

### 2.1 Device and hardware setup

The KIT 3D USCT prototype is shown in Fig.1. The patient is lying in a prone position on the patient bed. The breast is imaged in a fixed setup in a water bath. The aperture with 2041 transducers surrounds the breast. Due to no breast deformation and defined patient positioning, the volume images of the female breast are reproducible.

The device has a semi-ellipsoidal aperture with 628 emitters and 1413 receivers. Approx. spherical wave fronts are generated by each emitter at 2.5 MHz (approx. 50% bandwidth). Rotational and translational movement, so-called aperture positions, of the complete sensor system creates further virtual positions of the ultrasound transducers. The aperture in form of a semi-ellipsoid was optimized in respect to the isotropy of the 3D point spread function (PSF), the image contrast and the illumination [8]. An overview of the specifications of the KIT 3D USCT is given in Table 1 (all errors are given as standard deviations).

Sound pressure is generated and received using lead-zirconate titanate (PZT) composites. One quadratic module of PZT composite contains nine receivers and four emitters. Each transducer array is embedded including its pre-amplifier and control electronics in a Transducer Array System (TAS) casing. Each TAS contains a temperature sensor for tracking the temperature distribution and shift at 157 positions during measurements.

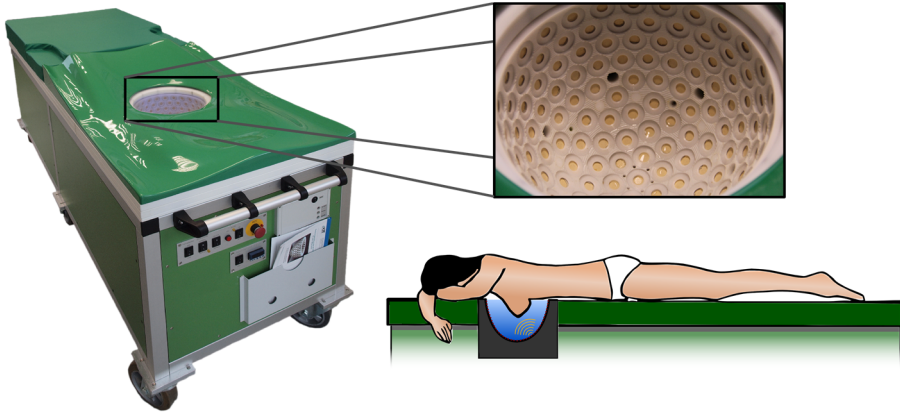


Figure 1: Left: KIT 3D USCT patient bed. Top right: Detail view of transducer aperture with 157 transducer array systems (TAS) containing 4 emitters and 9 receivers each. Bottom right: patient positioning on the patient bed during data acquisition. The breast is suspended freely in a water bath.

Type of specification	Value
No. parallel channels	480
Digitization	20 MHz @ 12 bit
On-board memory	80 GByte
Multiplex factor	3
Multiple sampling	1 to 128
No. TAS	157
No. emitters	628
No. receivers	1,413
Diameter TAS	28 mm
Emitters / TAS	4
Receivers / TAS	9
Receiver channels / TAS	3
Area individual transducer	$(0.9 \text{ mm})^2$
No. sub-elements / transducer	2 x 2
Area sub-element	$(0.4 \text{ mm})^2$
Max. excitation voltage	80 V
Opening angle	$38.2^\circ \pm 1.5^\circ @ -6 \text{ dB}$
Resonance frequency	$2.7 \pm 0.08 \text{ MHz}$
Bandwidth	$1.5 \pm 0.15 \text{ MHz} @ -6 \text{ dB}$
Sound pressure	$5.9 \pm 0.63 \text{ kPa} @ 12 \text{ cm}$

Table 1: Specification of KIT 3D USCT

Additionally, two calibrated PT100 temperature sensors are embedded in the TAS holder to enable increased accuracy. The measured temperature distribution can be applied during the image reconstruction to estimate the distribution of the speed of sound in the contact medium water.

The data acquisition is carried out with an FPGA based system, which can store up to 80 *GByte* of A-scans [10]. The system is housed in a 19" crate with a central processing board containing the control of the transducers, free programmable pulse shape of the transducer, and control of the system by a PCI Mezzanine Card (PMC) handling all input and output tasks of the crate. The PMC is a 1.4 *GHz* Pentium M board running Linux as operational system and supports a fast Ethernet interface and has a SATA interface to a solid state drive for storage of the measured data. The crate contains beside the central processing board 20 data acquisition boards (FLT). Each FLT contains 24 receiver channels, summing up to 480 channels processed simultaneously in the system and enabling data acquisition at one aperture position in approx. ten seconds. The digitalization is performed by three 8-fold (12 *Bit* @ 20 *MHz*) ADCs per board. After digitization, the parallel data streams are processed by FPGAs. The data streams are bandpass filtered (1.67 to 3.33 *MHz* @ -60 *dB*) and the data rate is reduced by a factor of 6, performing bandpass under-sampling. Using this approach, it is possible to store up to 47 data sets at different aperture positions in one data acquisition process in the internal memory buffer.

The aperture is realized as semi-elliptical TAS holder. The TAS holder is the container for the contact medium water and has several openings for water supply and drainage. The semi-elliptical aperture has a diameter of 26 *cm* and a height of 18 *cm*. The whole device is embedded in a patient bed as shown in Fig. 1 with a length of 2 *m*, a width of 70 *cm* and a height of 90 *cm*. It holds the aperture connected to the data acquisition hardware, translation- and rotation mechanics and motors, power supplies, water reservoir and heating, and disinfection system. It is covered by a mattress and serves as examination couch.

A 3D system requires a large number of transducers approx. two orders of magnitude more than a 2D system. The technical feasibility limits the number of transducer positions resulting in a sparse aperture and causing artefacts due to grating lobe effects in the resulting images [11]. A ring aperture requires a transducer distance smaller than  $0.5 \lambda R/r$ , where  $R$  is the radius of the ring and  $r$  the radius of the ROI [12]. A semi-spherical aperture leads to an upper limit of  $(2 \pi r/\lambda)^2$  transducers [13], if a uniform 1D sampling for the azimuth and elevation angles is applied.

For an exemplary ring system with radius 11.5 *cm* (see Table III) 103 *GByte* of raw data per breast have to be processed. To record, store and process this data is certainly challenging but feasible today. For a fully sampled sphere of this size the number of transducers, i.e.  $10^5$ , and the amount of data, i.e. 40 *TByte*, to be processed are no longer feasible.

Therefore, a compromise between the number of transducers and the image quality has to be made, i.e. contrast between image content and grating lobe artefacts. A quantification of the signal-to-artefact ratio for the KIT 3D USCT can be found in [11].

## 2.2 Image reconstruction

The applied reconstruction algorithm for reflectivity images is the 3D synthetic aperture focusing technique (SAFT). SAFT calculates at each image point the mean of all reflections which might originate from this position. For the simplest reconstruction, the harmonic mean of the speed of sound may be assumed to be constant, e.g. the speed of sound of water at the temperature measured during image acquisition. Alternatively, more accurate estimations of the speed of sound distributions, e.g. a speed of sound map calculated from the recorded transmissions, can be applied [14]. Correcting for the attenuation can be similarly estimated from the attenuation map of the breast [15].

The speed of sound and attenuation are reconstructed using a ray-based approach. The transmission signals are detected and the time-of-flight and relative signal energy, respectively, are applied in an algebraic reconstruction technique (ART) to calculate the resulting images. A compressive sensing algorithm, i.e. a 3D adaption of total variation minimization (TVAL3) is employed for optimization [16].

The computing system for reconstruction consists of a reconstruction PC (4 x AMD Opteron Octacore, 2.3 GHz, 256 GB RAM) and an external crate for Graphical Processor Units (GPU) (One Stop Systems) is connected via a second-generation PCI-Express bus. The external GPU crate is equipped with four Nvidia Geforce GTX 590 cards, with two GF100 GPUs per card. This results in a total number of eight separate GPUs for image reconstruction [17]. A time of flight interpolation based GPU implementation (TOFI-SAFT) [18] was developed which accelerates our previous GPU implementation of speed of sound corrected SAFT by a factor of 7 with only minor reduction of image quality. The approximation allows reconstructing speed of sound and attenuation corrected SAFT images as fast as non-corrected SAFT. A speed of sound and attenuation corrected SAFT volume of  $444^2 \times 266$  voxels, with  $128^3$  resolution of the attenuation and SOS maps and  $10^7$  A-scans can be calculated in 9 min. on eight GPU Titan.

The resulting reflectivity, speed of sound and attenuation images can be viewed separately, directly overlaid or overlaid with an applied threshold. The direct overlay codes the speed of sound or attenuation in a color map and the reflectivity as grey values. The overlay is done by adding the color-coded image to the grey image with an adjustable degree of transparency. The thresholded-fused image follows the method in [6], where a color image only marks image areas where the speed of sound and attenuation are above given thresholds, and then is overlaid on top of the reflectivity volume.

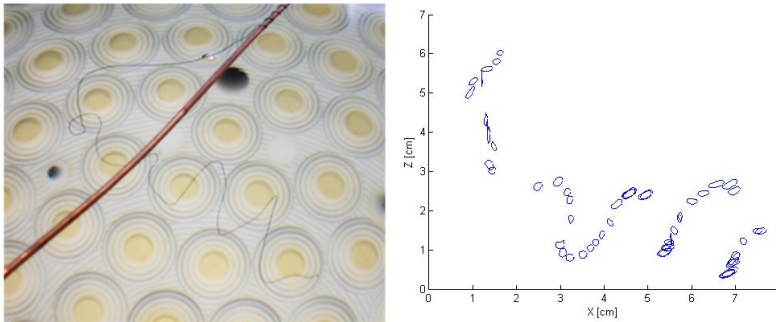


Figure 2: Bonding wire for PSF assessment. Left: photo. Right: 2D profiles at the evaluation points and their direction and position in space. Scaled up to a factor 3 for better visibility.

For comparison with other breast imaging modalities image registration may be applied. This enables direct comparability on a voxel to voxel basis, either for convenient viewing by radiologists or even for automatic analysis. Examples of MRI to USCT registration [19] are given in the results section, results of an evaluation of tissue classification using USCT to X-ray mammography registration is given in [20].

### 3 Imaging properties and clinical study

The predicted performance of the system, i.e. low spatial variance and isotropy of the 3D PSF, was evaluated in terms of FWHM [21]: A bonding wire with a diameter of  $0.07\text{ mm}$ , i.e. much thinner than the theoretical resolution of the system, was manually twisted into a helical structure within a bounding box of  $5.2\text{ cm} \times 4.3\text{ cm} \times 6.5\text{ cm}$ , so that the FWHM could be measured from many directions, see Fig. 2. The overall mean of the measured FWHMs was  $0.24\text{ mm} \pm 0.05\text{ mm}$ , fitting very well the predicted resolution of  $0.22\text{ mm}$ . The spatial variability was low, i.e. the standard deviation of the mean FWHM was measured at  $36\text{ }\mu\text{m}$  (predicted:  $35\text{ }\mu\text{m}$ ). The 3D global point spread function was measured with nearly isotropic diameters of  $dx,y,z = (0.2, 0.26, 0.24)\text{ mm}$ , (predicted:  $(0.2, 0.2, 0.25)\text{ mm}$ ).

The influence of a sparse 3D aperture on the contrast of reflectivity images was tested on simulated and real data in [11]. The main results were that the background noise due to grating lobes is mainly influenced by the sparsity of the aperture and the imaged object. For experimental data with the 3D USCT II prototype the amount of data acquired at ten aperture positions were empirically found to be a good compromise between data acquisition time and contrast. Fig. 3, left, shows example reconstructions for a healthy volunteer: whereas the contrast of the images increases from adding more data up to eight aperture positions, the increase of contrast using data from 16 aperture positions is only small. Fig. 3, right, shows a comparison of reconstructions of a breast phantom with the same amount of data, but differ-

ent transducer combinations. Whereas the left slice was reconstructed using transducers in a regular sampling pattern, the reconstruction of the right slice used from a large amount of different aperture positions the most irregularly spaced transducer combinations. The increase in contrast is significant. This property of a sparse aperture will be applied in the next generation system [21].

The first clinical study with the 3D USCT II device was conducted at the University Hospital in Jena (Germany). Ten patients were imaged. The primary aims of the study were to test the data acquisition and image reconstruction protocols, the fused display of the multimodal USCT images and the process of data acquisition and its optimization.

The patients included in the study were acquired during the standard MRI examination at the University Hospital Jena. The average age of the ten patients was 55.6 years ( $\pm 13.5$  years). The youngest patient was 37 years and the oldest 78 years. They first had their scheduled MRI examination and were then - if they met the inclusion criteria - asked to participate in the study. If they agreed, the USCT image acquisition was carried out directly after the MRI, so that the MRI images could be used as ground truth for comparison to the USCT volumes. The patient was asked to disinfect her breasts. Then she lay on the patient mattress and positioned the first breast into the USCT device. The central positioning of the breast was monitored and corrected using a B-scan like preview. Then the data acquisition for this breast was started. The same process was, if applicable, repeated for the second breast. At the end the patient was asked to fill a questionnaire to rate the imaging procedure. Before the next patient was examined, the data was read out onto a hard disc, the water was exchanged and the device disinfected.

For emission a linear frequency coded chirp with 2.5 MHz center frequency, 1 MHz bandwidth and 12.8  $\mu$ s duration was employed. Patients with breast lesions were imaged with ten aperture positions. For two patients, who were diagnosed with large cancer masses, the breasts with lesions were imaged with 13 aperture positions.

During the pilot study we could image approximately one patient per hour, which fitted quite well into the clinical process. For preparation of the device and patient information we needed between 15 and 30 min. The patient positioning took approx. 2 to 5 min. per breast and the image acquisition in sum 11 min.

In the meantime, the data was read out (14 min), the device was disinfected and the water was exchanged, sterilized and heated (approx. 15 min). The data acquisition time is mainly dominated by the time to move the aperture between different aperture positions. This time is depending on the path to be travelled. The mean time for DAQ with one movement during the pilot study was 50 s, i.e. 10 s DAQ plus 40 s aperture motion. In the meantime patient positioning and aperture movement could be accelerated by a factor two.

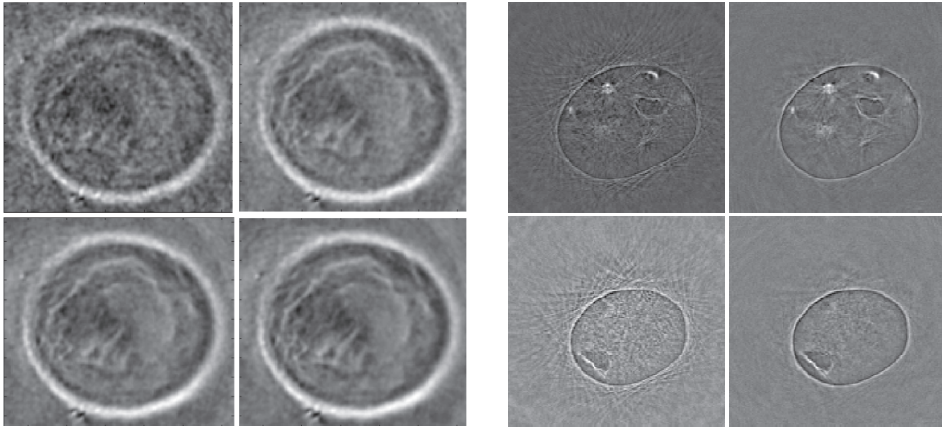


Figure 3: Left: 38-year-old healthy volunteer with an A cup: reconstructions of a frontal slice for one, four, eight and sixteen aperture positions from top left to bottom right. The slices are 11 cm by 12 cm and 3 cm inside the breast measured from the nipple position. Right: Slices of a CIRS multimodality breast phantom with the same amount of data, but with regular (left) and irregular (right) transducer spacing.

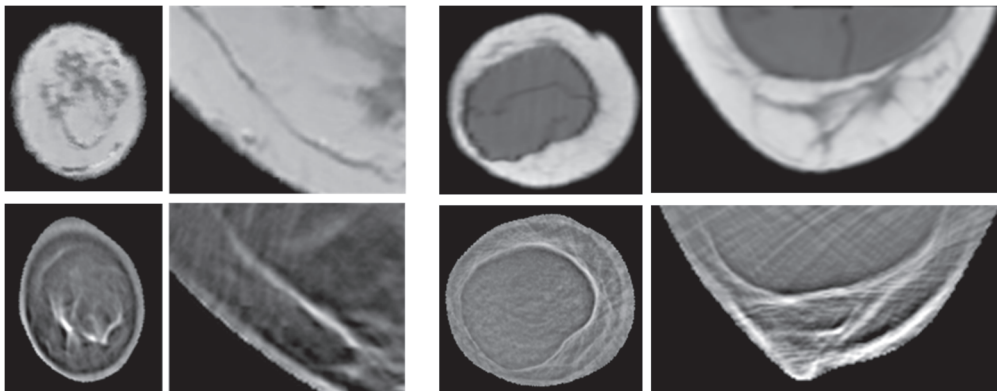


Figure 4: Top row: Registered native MRI in planar and transversal planes. Bottom row: USCT reflectivity slices at same positions. Left: Healthy patient. Right: 58-year-old patient with intact silicone implants (right breast).

Patient motion [23] was tracked in successive reflectivity reconstructions of full breast volumes for each aperture position. The mean distance between initial and final position was 2.2 mm ( $\pm 0.9$  mm) and the average sum of all moved distances was 4.9 mm ( $\pm 1.9$  mm). The tracked movement was corrected by summing successive images, which were transformed according to the detected motion.

Clinical data is shown in Fig. 4 and 5. All MRI volumes were registered to the USCT results so that direct spatial correspondence of the slices was archived [24].

Fig. 4 (left) shows native MRI slices and USCT reflectivity slices of a healthy patient to indicate the similarities of some tissue structures, Fig. 4 (right) the comparison of MRI and USCT reflectivity of a breast with an intact silicone implant. Fig. 5 shows cancer cases: for both cases registered MRI subtraction volumes are shown, indicating the tumor positions by a high content of contrast agent. The left case shows USCT reflectivity superposed with color-coded speed of sound and the right superposed with speed of sound thresholded at 1500 *m/s*. In both cases areas of high speed of sound in red are present at the approximately same positions as high amounts of contrast agent in the MRIs.

## 4 Conclusion and future work

We developed an optimized, unfocused 3D USCT with approximately isotropic 3D PSF and presented first images which demonstrate the performance of the system. We realized a sparse 3D USCT setup, resulting in homogeneous illumination, and nearly isotropic 3D PSF.

Image reconstructions with a wire and a clinical phantom confirm this: Currently, the mean FWHM in three dimensions is 0.24 *mm* with low dimensional and spatial deviation. The contrast of the reconstructed 3D volume of a breast phantom is very satisfactory in spite of our sparse aperture. The resolution is comparable to the high-quality MRI volume.

It seems that speed of sound is at the current state the most indicating modality for cancer. The spatial resolution of speed of sound and attenuation is currently limited by the ray based reconstruction algorithm in the range of 5 to 12 *mm*. Yet, this needs further evaluation. More complex reconstruction methods for transmission tomography leading to higher resolution are under development.

Patient positioning is crucial for imaging with our system. Displacements in the (transversal)  $x - y$  plane cause the illumination of the breast to vary strongly. Displacement in  $z$  (antero-posterior) direction leads to suboptimal coverage of the breast; the proximal part of the breast is then not imaged. Patient motion seems to be a minor problem; no definite movements between reconstructions of the single aperture positions could be detected. Breathing movement of the patients seems to have no effect on the images of the breast. The duration of the now improved data acquisition to 6 min per breast seemed to be acceptable for the patients. The process of breast examination with USCT was described as relatively comfortable by the patients.

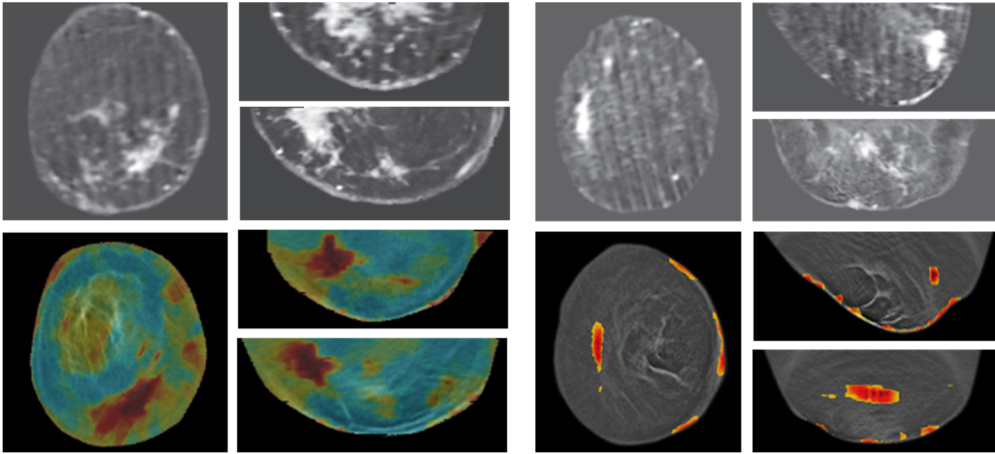


Figure 5: Top row: Registered MRI subtraction slices in planar, sagittal and transversal planes. Bottom row: USCT fusion slices at same positions. Left: 64-year-old patient with a large breast cancer in the left breast. Speed of sound is color coded and superposed on the reflectivity volume. Red colors indicate high speed of sound. Right: 74-year-old patient with breast cancer in the left breast. Speed of sound is thresholded at 1500  $m/s$  and overlaid on the reflectivity volume.

The next step in this work is to carry out a large clinical study and built a new 3D USCT system with higher contrast for reflection and position resolution for transmission tomography, shorter data acquisition time and a better access to the chest wall.

## References

- [1] H. Schomberg, *An improved approach to reconstructive ultrasound tomography*, J. Phys. D: Appl. Phys. 11, 1978.
- [2] M. Nguyen, H. Bressmer, et al., *Improvements in ultrasound transmission computed tomography*, Proc. European Conference on Engineering and Medicine, pp. 189190, 1993.
- [3] M. Ashfaq, and H. Ermert, *A new approach towards ultrasonic transmission tomography with a standard ultrasound system*, Proc. IEEE UFFC Symp., vol. 3, pp. 184851, 2004.
- [4] S. Mensah, P. Lasaygues, E. Debieu, and E. Franceschini, *AN AIS: An ultrasound mammograph*, Journal of the Acoustical Society of America, vol. 123, no. 5, pp. 30023002, 2008.
- [5] R. Stotzka, J. Würfel, T.O. Müller, and H. Gemmeke, *Medical imaging by ultrasound computer tomography*, Proc. SPIE Med. Imag., pp. 110-119, 2002.

- [6] N. Duric, P. Littrup, P. Chandiwala-Mody, C. Li, S. Schmidt, L. Myc, O. Rama, L. Bey-Knight, J. Lupinacci, B. Ranger, A. Szczepanski, and E. West, *In-vivo imaging results with ultrasound tomography: Report on an ongoing study at the Karmanos Cancer Institute*, Proc. SPIE Med. Imag., vol. 7629, pp. 76290M, 2010.
- [7] J. Wiskin, D. Borup, S. Johnson, M. Berggren, D. Robinson, J. Smith, J. Chen, Y. Parisky, J. Klock, *Inverse scattering and refraction corrected reflection for breast cancer imaging*, Proc. SPIE Med. Imag., vol. 7629, pp. 76290K, 2010.
- [8] G. Schwarzenberg, M. Zapf, and N.V. Ruiters, *Aperture optimization for 3D ultrasound computer tomography*, Proc. IEEE UFFC Symp., pp. 1820-1823, 2007.
- [9] J.F. Greenleaf, R.C. Bahn: *Clinical Imaging with Transmissive Ultrasonic Computerized Tomography*, IEEE Transactions on Biomedical Engineering 28(2), 177–185, 1981.
- [10] A. Kopmann, T. Bergmann, H. Gemmeke, M. Howe, M. Kleifges, A. Menshikov, D. Tcherniakhovski, J.F. Wilkerson, and S. Wuestling, *FPGA-based DAQ system for multi-channel detectors*, Proc. IEEE NSS MIC, 2008.
- [11] N.V. Ruiters, M. Zapf, T. Hopp, and H. Gemmeke, *Experimental evaluation of noise generated by grating lobes for a sparse 3D ultrasound computer tomography system*, Proc. SPIE Med. Imaging, 2013.
- [12] F. Simonetti, L. Huang, and N. Duric, *On the sampling of wave fields with circular ring apertures*, Journal of applied physics, vol. 101, 2007.
- [13] F. Simonetti, and L. Huang, *Synthetic aperture diffraction tomography for three-dimensional imaging*, Proc. R. Soc. A, 465, 2009.
- [14] E. Kretzek, and N.V. Ruiters, *GPU based 3D SAFT reconstruction including phase aberration*, Proc. SPIE 9040, Medical Imaging 2014: Ultrasonic Imaging and Tomography, pages 90400W (2014).
- [15] E. Kretzek, T. Hopp, and N.V. Ruiters, *GPU-based 3D SAFT reconstruction including attenuation correction*, Proc. SPIE 9419, Medical Imaging 2015: Ultrasonic Imaging and Tomography, pages 94190E (2015).
- [16] R. Dapp, M. Zapf, and N.V. Ruiters, et al., *Geometry Independent Speed of Sound Reconstruction for 3D USCT Using Apriori Information*, Proc. IEEE UFFC Symp., pp. 1403-1406, 2011.
- [17] E. Kretzek, M. Zapf, M. Birk, H. Gemmeke, and N.V. Ruiters, *GPU based acceleration of 3D USCT image reconstruction with efficient integration into MATLAB*, Proc. SPIE Med. Imag. 8675 (2013) 86750O.
- [18] N.V. Ruiters, E. Kretzek, M. Zapf, T. Hopp, and H. Gemmeke, *Time of flight interpolated synthetic aperture focusing technique*, Proc. SPIE 10139, Medical Imaging 2017: Ultrasonic Imaging and Tomography, 101390Q (2017).

- [19] T. Hopp, R. Dapp, M. Zapf, E. Kretzek, H. Gemmeke, and N.V. Ruiter, *Registration of 3D ultrasound computer tomography and MRI for evaluation of tissue correspondences*, Progress in Biomedical Optics and Imaging - Proceedings of SPIE, 2015.
- [20] T. Hopp, N. Duric, and N.V. Ruiter, *Image Fusion of Ultrasound Computer Tomography Volumes with X-Ray Mammograms using a Biomechanical Model Based 2D/3D Registration*, Computerized Medical Imaging and Graphics, 40, 2014.
- [21] N.V. Ruiter, M. Zapf, and H. Gemmeke, *Evaluation of 3D point spread function of a semi-ellipsoidal ultrasound computer tomography system*, Proc. IEEE UFFC Symp., 2011.
- [22] N.V. Ruiter, M. Zapf, T. Hopp, R. Dapp, and H. Gemmeke, *Optimization of the aperture and the transducer characteristics of a 3D Ultrasound Computer Tomography System*, Proc. SPIE Medical Imaging: Ultrasonic Imaging and Tomography, 2014.
- [23] N.V. Ruiter, T. Hopp, M. Zapf, E. Kretzek, H. Gemmeke, *Analysis of patient movement during 3D USCT data acquisition*, Proc. SPIE Med. Imag. 9790, 97900A, 2016.
- [24] T. Hopp, L. Sroba, M. Zapf, R. Dapp, E. Kretzek, H. Gemmeke, and N.V. Ruiter, *Breast Imaging with 3D Ultrasound Computer Tomography: Results of a First In-vivo Study in Comparison to MRI Images*, H. Fujita, T. Hara, and C. Muramatsu (Eds.): IWDM 2014, LNCS 8539, pp. 72–79, 2014.